LASER
& PHOTONICS
REVIEWS

Supporting Information

for *Laser Photonics Rev.*, DOI 10.1002/lpor.202400387

High-Speed High-Resolution Transport of Intensity Diffraction Tomography with Bi-Plane Parallel Detection

Ning Zhou, Runnan Zhang, Weisheng Xu, Ruizhi Zhu, Hanci Tang, Xiao Zhou, Jiasong Sun, Peng Gao, Qian Chen* and Chao Zuo**

Supporting Information for High-speed high-resolution transport of intensity diffraction tomography with bi-plane parallel detection

Ning Zhou[1,2,3], Runnan Zhang[1,2,3], Weisheng Xu[1,2,3], Ruizhi Zhu[1,2,3], Hanci Tang[1,2,3], Xiao Zhou[1,2,3], Jiasong Sun[1,2,3], Peng Gao[4,*], Qian Chen[2,3,*], and Chao Zuo[1,2,3,*]

[1]Smart Computational Imaging Laboratory (SCILab), School of Electronic and Optical Engineering, Nanjing University of Science and Technology, Nanjing, Jiangsu 210094, China
[2]Smart Computational Imaging Research Institute (SCIRI) of Nanjing University of Science and Technology, Nanjing, Jiangsu 210019, China
[3]Jiangsu Key Laboratory of Spectral Imaging & Intelligent Sense, Nanjing University of Science and Technology, Nanjing, Jiangsu 210094, China
[4]School of Physics, Xidian University, Xi'an, China
[1]Ning Zhou, Runnan Zhang, and Weisheng Xu contributed equally to this work
[*]Address all correspondence to Peng Gao,peng.gao@xidian.edu.cn, Qian Chen,chenqian@njust.edu.cn, Chao Zuo, zuochao@njust.edu.cn

ABSTRACT

This document provides supplementary information for "High-speed high-resolution transport of intensity diffraction tomography with bi-plane parallel detection".

Contents

Supporting Information S1. Defocus distance selection analysis

As described in the manuscript, the BP-TIDT method encodes the low-frequency phase information lost due to mismatched illumination into the intensity image through defocus modulation. In **Section 2** of the main text, we detailed how to reconstruct the 3D RI of the sample using data from two different focal planes. The experimental results in Fig. S1(a1) show that images with symmetrically separated smaller defocus distances can reconstruct the high-frequency components of the RI with high quality (the filopodia of HepG2 cells within the white circle are visible). Nevertheless, there is a slight lack of low-frequency components (the cell nucleus and the overall cell contour indicated by the white arrow are not prominent). In contrast, as shown in Fig. S1(a2), images with more considerable defocus distances can reconstruct the low-frequency components well (such as the overall cell contour and the cell nucleus indicated by the white arrow are visible). However, the high-frequency components are still lost (the filopodia within the white circle are not visible due to high-frequency noise). Therefore, to ensure spatial resolution while obtaining better low-frequency reconstruction results with the BP-TIDT method, we need to analyze and discuss the defocus distance from the perspective of the PTF.

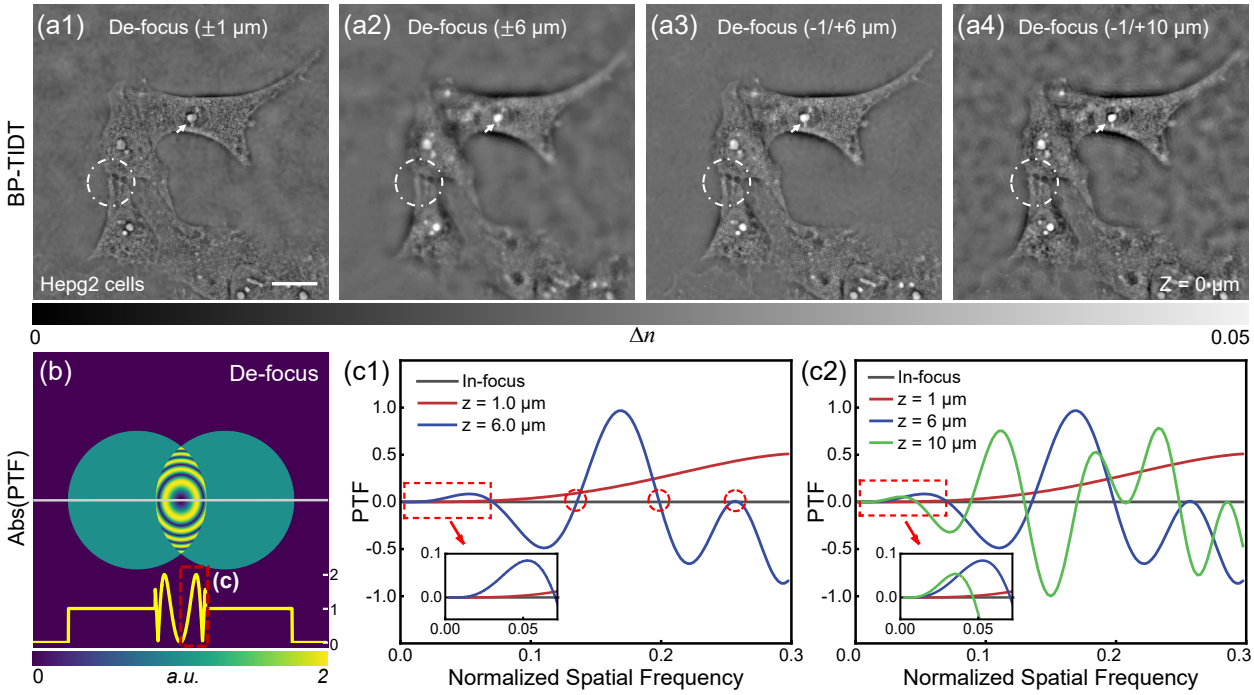

Figure S1. Analysis of defocus distance selection. (a1)-(a4) Reconstruction results of HepG2 with different defocus schemes. (b) Absolute value distribution of the two-dimensional phase transfer function (PTF) under mismatched illumination and defocused plane conditions. (c1)-(c2) PTF corresponding to different defocus distances.

As described in **Section 2.2** of the main text, since defocus is an energy transfer process[1], the absolute value of the phase distribution in the non-overlapping region remains unchanged compared to the

focused condition, so we only analyze PTF in the red dashed box area in Fig. S1(b). As shown in Fig. S1(c1), under coherent illumination, the response curve of the PTF will offer an increasingly accelerated oscillating distribution as the defocus distance increases, leading to multiple zero-crossings in the curve (indicated by the red circles in the figure). Zero-crossings are not conducive to recovering high-frequency phase components during the reconstruction process. When the defocus is small, the PTF can be approximated as a linear function related to the frequency coordinate **u**, effectively avoiding function oscillation, but this also leads to a decrease in low-frequency phase contrast[2]. It is difficult to obtain high signal-to-noise ratio reconstruction results, especially for low spatial frequency components such as cell contours or more prominent cellular organelles within the cell. The analysis results of the transfer function correspond to the results of HepG2 cells in Figs. S1(a1) and (a2). Therefore, to restore high-quality results, we adopt two sets of intensity images with asymmetric defocus distances in the BP-TIDT method to synthesize and optimize the PTF, ensuring resolution while obtaining better low-frequency reconstruction effects, as shown in Fig. S1(a3). It should be noted that, due to the aberrations between the actual imaging system and the theoretical reconstruction model, as well as the marginal effect of the low-frequency enhancement (as shown in the subgraph of Fig. S1(c2)), it is not possible to enhance the low-frequency by infinitely increasing the defocus distance. The high-frequency part will rapidly oscillate and attenuate with increasing defocus distance, leading to an increase in high-frequency noise in the reconstruction RI (as shown in Fig. S1(a4)). Therefore, we chose $\Delta z = -1$ μm and $\Delta z = 6$ μm in our previous experiments.

The theoretical analysis and experimental results suggest that simultaneously collecting small and large defocus images under asymmetric defocus distances provides new possibilities to push the resolution limit and improve the low-frequency performance of BP-TIDT imaging. However, due to the complicated form of the PTF under tilted illumination in 3D diffraction tomography, solving an optimal imaging system scheme that considers both the illumination NA and defocus distance is quite challenging. The current selection of defocus distance is based on empirical design combined with intuitive standards related to the shape of the PTF and experimental results. Enabling more elaborate criteria (merit functions) to evaluate the "goodness" of the defocus distance and optimize imaging results based on optimization algorithms are interesting directions for future work.

Supporting Information S2. Analysis of illumination schemes for 3D dynamic imaging

In dynamic imaging processes, to visualize 3D living samples with minimal motion-related artifacts, it is necessary to choose an appropriate illumination scheme while reducing exposure time. Based on ring-shaped LED illumination, this section further optimizes the illumination scheme through simulation to determine the number of LEDs required for illumination. Figure S2 shows the simulated reconstruction results of a 6 μm diameter polystyrene microsphere under different illumination modes. To simulate the experimental platform realistically, the imaging system and sample parameters utilized in the simulation

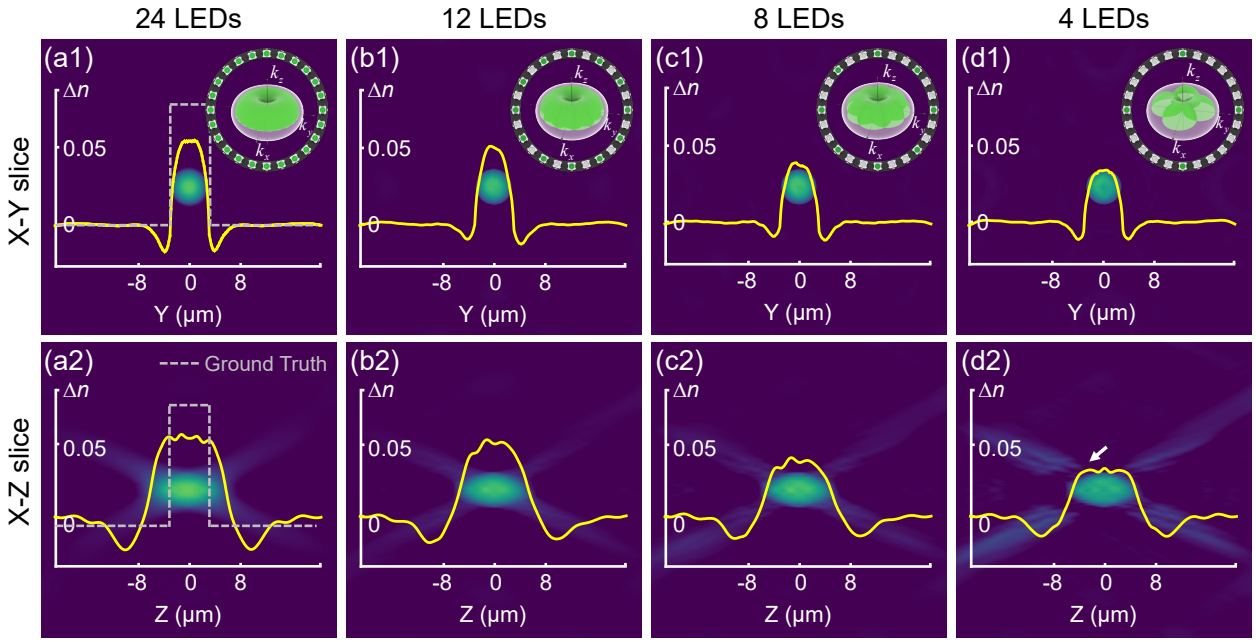

Figure S2. Reconstruction results under different illumination modes. (a1)-(d1) Transverse slices of a 6 μm diameter polystyrene microsphere reconstructed from 24, 12, 8, and 4 images, along with the corresponding 3D frequency spectral filling conditions for each illumination mode. (a2)-(d2) Axial slices of the reconstructed microsphere under different illuminations.

are consistent with **Section 2.1** of the main text. As shown in Fig. S2(a), we first used 24 LEDs as the illumination scheme for image acquisition and reconstruction, and the results obtained were almost identical to the input original data. Additionally, the 3D frequency spectral filling condition in Fig. S2(a1) also indicates that the 3D spectrum can be effectively filled when there is sufficient data redundancy, achieving isotropic resolution in the transverse direction. It should be noted that although the refractive index reconstructed in the experiment is consistent with the simulation results, we still found that it is somewhat underestimated compared to the true value. In addition, we observed a significant stretching phenomenon of the sample in the z-axis direction. This is due to the missing cone problem inherent in the LED angle-scanning ODT technology[3,4]. As the number of illumination LEDs is gradually reduced, the reconstruction results shown in the transverse and axial slices still have similar distributions, as shown in Figs. S2(b)-(c). However, the filling rate of the 3D frequency spectrum will gradually decrease with the reduction of LED numbers, and the reconstructed RI will be underestimated due to the missing spectrum, which needs to be considered in the subsequent algorithm for compensation.

Reducing the number of LEDs to four leads to significant artifacts and distortions, as indicated by the white arrows in Fig. S2(d2), rendering the reconstruction results unsatisfactory. The 3D frequency spectrum filling condition in Fig. S2(d1) also indicates that this illumination scheme has insufficient data redundancy, leading to an anisotropic resolution in the transverse slices. The simulation results show that at least 8 raw images can provide better data support for solving the problem. It should be noted that

in the actual imaging process, reducing the number of LEDs used decreases data redundancy, making the reconstruction results more sensitive to noise and errors. Therefore, in dynamic experiments with living cells, we must combine the LED position calibration algorithm[5] with system aberration correction methods[6] proposed in our previous work to calibrate the transfer function, optimizing the imaging results while improving temporal resolution.

Supporting Information S3. Transfer function theory for two-dimensional imaging

For two-dimensional (2D) thin samples in quantitative phase imaging (QPI), the object is described by a 2D complex amplitude function $O(\mathbf{r}) = A(\mathbf{r})\exp[j\phi(\mathbf{r})]$, where $A(\mathbf{r})$ and $\phi(\mathbf{r})$ represent the absorption and phase components of the sample respectively, with $\mathbf{r}$ is a short-hand notation for the spatial coordinate. Assuming the sample is illuminated by a quasi-monochromatic plane wave with unit amplitude, the total field $U(\mathbf{r})$ can be considered as the coherent superposition of the incident field $U_{in}(\mathbf{r})$ and scattered field $U_s(\mathbf{r})$, i.e.,$U(\mathbf{r}) = U_{in}(\mathbf{r}) + U_s(\mathbf{r})$. Under the assumption of generality, we represent the contribution of the target as a complex phase function $\varphi_s(\mathbf{r})$, with the form[7]:

$$\begin{aligned}\varphi_s(\mathbf{r}) &= \ln\left[U(\mathbf{r})/U_{in}(\mathbf{r})\right] = \ln\left[1 + U_s(\mathbf{r})/U_{in}(\mathbf{r})\right] \\ &\equiv a(\mathbf{r}) + j\phi(\mathbf{r})\end{aligned} \tag{S1}$$

For 2D imaging, the significance of the complex phase function $\varphi_s(\mathbf{r}) = \ln A(\mathbf{r}) + j\phi(\mathbf{r}) = a(\mathbf{r}) + j\phi(\mathbf{r})$ is evident, where the $a(\mathbf{r})$ and $\phi(\mathbf{r})$ represent the sample's real (absorption) and imaginary (phase) components respectively. In previous work, we provided a linearized relationship between the first-order scattered field and the target function under the first-order Born or Rytov approximation:

$$\hat{O}(\mathbf{u} - \mathbf{u}_{in}) = \hat{U}_{s1}(\mathbf{u})P(\mathbf{u}) \tag{S2}$$

where $U_{s1}(\mathbf{r}) = U_{in}(\mathbf{r})\varphi_s(\mathbf{r})$ stands for the first-order scattered field of the sample, $\hat{O}$ and $\hat{U}_{s1}$ are the 2D Fourier transforms of O and U_{s1} respectively. $P(\mathbf{u})$ is the 2D complex pupil function [i.e., the 2D coherent transfer function (CTF)], which ideally is a circular function with a radius NA_{obj}/λ determined by the NA of the objective lens. For 2D samples, the first-order scattered field provides the spectral information of the object within the displaced pupil function. Eq.S2 indicates that, for a given illumination angle, each measurement of the first-order scattered field $\hat{U}_{s1}$ only provides limited frequency information of the object determined by the illumination angle and the pupil function. Therefore, it is necessary to illuminate the object from different directions, i.e., adjust the incident light angle $\mathbf{u}_{in}$ to expand the accessible object spectrum, thereby reconstructing the complex amplitude of the 2D sample. For typical

microscope systems, the maximum allowable illumination angle is limited by NA_{obj}, and its maximum spectral coverage is the same as that of traditional non-coherent illumination microscopy. Compared with the coherent diffraction limit, it has doubled the lateral resolution ($2NA_{obj}/\lambda$). In traditional QPI systems, to determine the first-order scattered field $U_{s1}(\mathbf{u})$, the complex amplitude distribution (amplitude and phase) of the total field $U(\mathbf{u})$ is required, which usually involves interferometric or holographic measurements. However, for non-interferometric QPI methods, people attempt to retrieve the sample's phase distribution from the intensity of the total field measured, which can be directly expressed as:

$$I(\mathbf{r}) = |A(\mathbf{r})|^2 = |U(\mathbf{r})|^2 = |U_{\text{in}}(\mathbf{r})|^2 |\exp \varphi_{\text{s}}(\mathbf{r})|^2 = \exp\left[2\text{Re}\left[\varphi_{\text{s}}(\mathbf{r})\right]\right] \tag{S3}$$

According to Eq.S2 and $U_{s1}(\mathbf{r}) = U_{in}(\mathbf{r})\varphi_s(\mathbf{r})$, the complex phase function of the first-order scattered field under the Born or Rytov approximation can be written as:

$$\begin{aligned}
\varphi_s(\mathbf{r}) &= \frac{1}{U_{\text{in}}(\mathbf{r})} U_{s1}(\mathbf{r}) \\
&= \frac{1}{U_{\text{in}}(\mathbf{r})} \left[O(\mathbf{r}) U_{\text{in}}(\mathbf{r})\right] \otimes g(\mathbf{r}) \\
&= \frac{1}{U_{\text{in}}(\mathbf{r})} \left[a(\mathbf{r}) U_{\text{in}}(\mathbf{r})\right] \otimes g(\mathbf{r}) + \frac{j}{U_{\text{in}}(\mathbf{r})} \left[\phi(\mathbf{r}) U_{\text{in}}(\mathbf{r})\right] \otimes g(\mathbf{r})
\end{aligned} \tag{S4}$$

where $g(\mathbf{r})$ denotes the complex point spread function (PSF) of the imaging system. According to Eq.S4, the intensity image of the 2D measurement can be expressed as:

$$\begin{aligned}
&\ln[I(\mathbf{r})] = 2\text{Re}\left[\varphi_s(\mathbf{r})\right] \\
&= 2\text{Re}\left[\tfrac{1}{U_{\text{in}}(\mathbf{r})} \left[a(\mathbf{r}) U_{\text{in}}(\mathbf{r})\right] \otimes g(\mathbf{r}) + \tfrac{j}{U_{\text{in}}(\mathbf{r})} \left[\phi(\mathbf{r}) U_{\text{in}}(\mathbf{r})\right] \otimes g(\mathbf{r})\right] \\
&= 2\text{Re}\left[a(\mathbf{r}) \otimes g'(\mathbf{r})\right] + 2\text{Re}\left[j\phi(\mathbf{r}) \otimes g'(\mathbf{r})\right] \\
&= a(\mathbf{r}) \otimes 2\text{Re}\left[g'(\mathbf{r})\right] + \phi(\mathbf{r}) \otimes 2\text{Re}\left[jg'(\mathbf{r})\right] \\
&= a(\mathbf{r}) \otimes \left[g'(\mathbf{r}) + g'^*(\mathbf{r})\right] + \phi(\mathbf{r}) \otimes \left[g'^*(\mathbf{r}) - g'(\mathbf{r})\right] \\
&= a(\mathbf{r}) \otimes h_a(\mathbf{r}) + \phi(\mathbf{r}) \otimes h_p(\mathbf{r})
\end{aligned} \tag{S5}$$

where $g'(\mathbf{r})$ indicates the PSF modulated by the incident field U_{in}, $h_a(\mathbf{r})$ and $h_p(\mathbf{r})$ signify the PSF corresponding to the real (absorption) and imaginary (phase) components respectively. Taking the Fourier transform of both sides of Eq.S5, we obtain the logarithmic intensity spectrum:

$$\ln[\hat{I}(\mathbf{u})] = \hat{a}(\mathbf{u}) H_a(\mathbf{u}) + \hat{\phi}(\mathbf{u}) H_p(\mathbf{u}) \tag{S6}$$

where $\hat{I}(\mathbf{u})$, $\hat{a}(\mathbf{u})$ and $\hat{\phi}(\mathbf{u})$ are the Fourier spectrum of the $I(\mathbf{r})$, $a(\mathbf{r})$ real (absorption) and imaginary (phase) components. $H_a(\mathbf{u})$ and $H_p(\mathbf{u})$ are the transfer functions of the absorption and phase components, respectively. Under coherent illumination, $H_a(\mathbf{u})$ and $H_p(\mathbf{u})$ can be expressed as:

$$\begin{aligned} H_a(\mathbf{u}) &= P(\mathbf{u}+\mathbf{u}_{in}) + P^*(\mathbf{u}-\mathbf{u}_{in}) \\ H_p(\mathbf{u}) &= P^*(\mathbf{u}-\mathbf{u}_{in}) - P(\mathbf{u}+\mathbf{u}_{in}) \end{aligned} \tag{S7}$$

where $P(\mathbf{u}+\mathbf{u}_{in})$ is the Fourier transform of $g'(\mathbf{r})$, utilizing the shift property of the Fourier transform. $P(\mathbf{u})$ and $P^*(\mathbf{u})$ are the conjugate of the aperture function.

For 2D QPI of unlabeled biological samples, the phase component $\hat{\phi}(\mathbf{u})$ dominates the intensity contrast and is the quantity of interest. As shown in Figure 2(a) of the main text, for a perfectly focused imaging system, axial illumination ($\mathbf{u}_{in}=0$) does not produce phase contrast because the two asymmetric (positive and negative) pupils cancel each other out, indicating that phase structures cannot be observed under this condition. Increasing the illumination angle ($0<|\mathbf{u}_{in}|<NA_{obj}/\lambda$) causes the two pupils to no longer completely overlap, thereby making the phase information visible. However, only when the illumination angle matches the NA of the objective lens ($|\mathbf{u}_{in}|=NA_{obj}/\lambda$) can the low-frequency phase component (near zero frequency) be fully transferred. This matching illumination condition is crucial for the precise phase recovery of non-interferometric QPI methods based on asymmetric illumination, such as Fourier ptychographic microscopy (FPM)[8] and Transport of intensity equation (TIE)[9].

Supporting Information S4. Transfer function theory for three-dimensional imaging

S4.1. Relationship between two-dimensional complex amplitude and three-dimensional complex scattering potential

In the fundamental theory of diffraction tomography, the physical quantity to be inverted is the scattering potential of a thick three-dimensional (3D) sample, depicted as follows[10]:

$$O(\mathbf{r}) = k_0^2\left[n(\mathbf{r})^2 - n_m^2\right] \tag{S8}$$

where $k_0=2\pi/\lambda$ is the wave number, λ is the illumination wavelength in free space, $n(\mathbf{r})=n_{re}+i\cdot n_{im}$ and n_m are the spatial refractive index (RI) distributions of the sample and its surrounding medium, respectively. The real part of the sample's RI n_{re} describes the phase modulation properties of light passing through the sample, and the imaginary part n_{im} describes the modulation of absorption. $\mathbf{r}=(\mathbf{r}_T,z)=(x,y,z)$ is a shorthand notation for the 3D spatial coordinates, with the z-direction parallel to the microscope's objective lens. Without loss of generality, $z=0$ is the plane of the objective lens. We define

$\Delta\varepsilon(\mathbf{r}) = n(\mathbf{r}) - n_{\mathrm{m}}$ as the sample's dielectric constant, representing local variations in the internal RI, and assume that it is small. Thus, the complex scattering potential can be described as:

$$O(\mathbf{r}) = k_0^2 \left[\Delta\varepsilon_{\mathrm{Re}}(\mathbf{r}) + i\Delta\varepsilon_{\mathrm{Im}}(\mathbf{r})\right] \tag{S9}$$

where $\Delta\varepsilon = \Delta\varepsilon_{re} + i \cdot \Delta\varepsilon_{im}$, $\Delta\varepsilon_{re}$ refers to the phase effect on the object, and $\Delta\varepsilon_{Im}$ represents the effect of absorption.

For 3D imaging, the variation of the phase $\phi(\mathbf{r})$, which is experienced by the incident light $U_{in}(\mathbf{r})$ as it passes through the sample along a specific path s_{path}, can be approximated by ray optics[11]:

$$\phi(\mathbf{r}) \approx \frac{2\pi}{\lambda}\left(\int_{\mathrm{path}} ds_{\mathrm{path}} n_{\mathrm{Re}}(\mathbf{r}) - s_{\mathrm{tot}} n_{\mathrm{m}}\right) \tag{S10}$$

Since the measured samples in 3D diffraction tomography are typically transparent biological cells with negligible imaginary parts (absorption) of the RI, we neglect the imaginary part of the RI here. s is the approximate thickness of the sample. For a homogeneous sample with RI n_{s}, the absolute phase variation is calculated as:

$$\phi(\mathbf{r}) = \frac{2\pi}{\lambda} s\,(n_{\mathrm{s}} - n_{\mathrm{m}}) = \frac{2\pi}{\lambda} s\varepsilon_{\mathrm{n}} \tag{S11}$$

This equation can be interpreted as a comparison of phase change $\phi(\mathbf{r})$ over a period of 2 with the change of the optical path length $s\,(n_{\mathrm{s}} - n_{\mathrm{m}})$ over one wavelength λ.

Then write Eq.S11 in differential form, we express the total differential of $\phi(\mathbf{r})$ with respect to spatial distance s and RI variation ε_{n} as:

$$\frac{d(\phi(\mathbf{r}))}{2\pi} = \frac{\varepsilon_{\mathrm{n}}}{\lambda} ds + \frac{s}{\lambda} d\varepsilon_n \tag{S12}$$

The phase $\phi(\mathbf{r})$ is composed of two contributions from the sample: (1) the thickness of the sample:

$$\frac{d(\phi(\mathbf{r}))}{2\pi} = \frac{\varepsilon_{\mathrm{n}}}{\lambda} ds \tag{S13}$$

and (2) the RI variation inside the sample:

$$\frac{d(\phi(\mathbf{r}))}{2\pi} = \frac{s}{\lambda} d\varepsilon_n \tag{S14}$$

Note that in general ε_n is dependent on $\mathbf{r}(3D) = (x, y, z)$ and $\phi(\mathbf{r})$ is measured at the detector plane $\mathbf{r}(2D) = (x, y)$. If the RI of the sample is fixed, then the total phase $\phi(\mathbf{r})$ depends on the sample's thickness. Also, if the sample's thickness s is fixed, then the local variation of the RI within the sample determines the value of the absolute phase.

When the sample only modulates the phase of the transmitted field (given by $n_{re}(\mathbf{r})$), the function $O(\mathbf{r})$ is real in the lossless case, so the target function is $O(\mathbf{r}) = \Delta\varepsilon_{\mathrm{Re}}$. When considering the sample's absorption (given by n_{im}), the function $O(\mathbf{r}) = \Delta\varepsilon_{\mathrm{Re}} + i\Delta\varepsilon_{\mathrm{Im}}$ becomes a complex function[12], where $\Delta\varepsilon_{\mathrm{Re}} = k_0^2(n_{re}(\mathbf{r})^2 - n_{im}(\mathbf{r})^2 - n_m^2)$ and $\Delta\varepsilon_{\mathrm{Im}} = 2k_0^2 n_{re}(\mathbf{r}) n_{im}$. According to the Eq.S10, the complex phase function can be expressed as $\varphi_s(\mathbf{r}) = \Delta\varepsilon_{\mathrm{Im}} + i\Delta\varepsilon_{\mathrm{Re}}$, where $\Delta\varepsilon_{\mathrm{Im}}$ and $\Delta\varepsilon_{\mathrm{Re}}$ represent the imaginary (absorption) and real (phase) parts of the sample's complex scattering potential, respectively.

S4.2. The transfer function of three-dimensional imaging

Assuming that a 3D sample is illuminated by a quasi-monochromatic plane wave with unit amplitude, the total field $U(\mathbf{r})$ obtained can be considered as the coherent superposition of the incident field $U_{in}(\mathbf{r})$ and the scattered field $U_s(\mathbf{r})$[10]:

$$U(\mathbf{r}) = U_{in}(\mathbf{r}) + U_s(\mathbf{r}) \tag{S15}$$

Assuming the incident field is a plane wave:

$$U_{in}(x, y, z) = \sqrt{S(-k_{xi}, -k_{yi})}\, e^{\mathrm{i}\left(k_{xi}x + k_{yi}y + k_{zi}z\right)} \tag{S16}$$

where S stands for the 2D intensity distribution of the illumination source (in Kohler illumination), and (k_{xi}, k_{yi}, k_{zi}) indicates the spatial frequency of the incident field, satisfying:

$$k_{zi} = \sqrt{k^2 - k_{xi}^2 - k_{yi}^2} \tag{S17}$$

where k is the wave number in the surrounding medium. According to the first-order Born approximation, the scattered field can be expressed as:

$$U_S(\mathbf{r}) = \iiint U_{in}(\mathbf{r}')\, O(\mathbf{r}')\, G(\mathbf{r}-\mathbf{r}')\mathrm{d}\mathbf{r}' \tag{S18}$$

where G represents the Green's function, assuming our imaging system satisfies the homogeneous free-space approximation:

$$G(\mathbf{r}-\mathbf{r}') = \frac{\exp(ik_{\mathrm{m}}|\mathbf{r}-\mathbf{r}'|)}{4\pi|\mathbf{r}-\mathbf{r}'|} \tag{S19}$$

Using Weyl's expansion, this spherical wave Green's function can be represented in the form of angular spectrum representation:

$$G(\mathbf{r}-\mathbf{r}') = \frac{ik}{16\pi^3}\iint \frac{1}{s_z} e^{\mathrm{i}k\left[s_x(x-x')+s_y(y-y')+s_z|z-z'|\right]} ds_x s_y \tag{S20}$$

where (s_x, s_y, s_z) is the unit vector component, $s_x = k_x/k$, $s_y = k_y/k$, and $s_z = k_z/k$ are related to the spatial frequency variable (k_x, k_y, k_z) , with the axial spatial frequency k_z satisfying:

$$k_z = \sqrt{k^2 - k_x^2 - k_y^2} \tag{S21}$$

where the positive sign in k_z corresponds to the forward scattering component. Therefore, the Green's function can be rewritten as:

$$G(\mathbf{r}-\mathbf{r}') = \frac{i}{2\pi}\iint \frac{1}{k_z} e^{\mathrm{i}\left[k_x(x-x')+k_y(y-y')+k_z|z-z'|\right]} dk_x k_y \tag{S22}$$

where $|z-z'| = z-z'$, since our system only measures the forward scattering on the camera plane. Substituting Eqs.S16 and S22 into Eq.S18:

$$\begin{aligned} U_S(\mathbf{r}) = {} & \frac{i}{16\pi^3}\sqrt{S(-k_{xi},-k_{yi})}\iiint e^{\mathrm{i}\left(k_{xi}x+k_{yi}y+k_{zi}z\right)} O(\mathbf{r}') \\ & \iint \frac{1}{k_z} e^{\mathrm{i}\left[k_x(x-x')+k_y(y-y')+k_z|z-z'|\right]} dk_x k_y \mathrm{d}\mathbf{r}' \end{aligned} \tag{S23}$$

Then we calculate the total scattered field at the focal plane ($z = 0$) and integrate over dx' and dy' to obtain:

$$U_S(x,y,0) = \frac{i}{16\pi^3}\sqrt{S(-k_{xi},-k_{yi})}\int e^{\mathrm{i}k_{zi}z} \iint \frac{1}{k_z} e^{-\mathrm{i}k_z z'}\widehat{O}\left(k_x - k_{xi}, k_y - k_{yi}, z'\right) e^{\mathrm{i}\left(k_{xi}x + k_{yi}y\right)} dk_x k_y \mathrm{d}z' \tag{S24}$$

where $\hat{O}(k_x, k_y, z')$ represents the 2D Fourier transform (FT) of the axial slice of the sample at depth z', and $\widehat{\cdot}$ is the 2D FT operator. By neglecting the evanescent field components in $\widehat{O}$, the integrations over k_x and k_y can be replaced by inverse Fourier transforms (IFT):

$$U_S(x,y,0) = \frac{i}{16\pi^3}\sqrt{S(-k_{xi},-k_{yi})}\int e^{\mathrm{i}k_{zi}z} \mathscr{F}^{-1}\left\{\frac{e^{-\mathrm{i}\sqrt{k^2-k_x^2-k_y^2}z'}}{\sqrt{k^2-k_x^2-k_y^2}}\hat{O}\left(k_x - k_{xi}, k_y - k_{yi}, z'\right)\right\}\mathrm{d}z' \tag{S25}$$

where $\mathscr{F}^{-1}$ represents the two-dimensional IFT operator.

The focused intensity captured at the back focal plane of the microscope is:

$$I(x,y) = |U(x,y,0) * h(x,y)|^2 \tag{S26}$$

where $U(x,y,0)$ is the total field on the front focal plane, $h(x,y)$ is the microscope's point spread function (PSF), and $*$ denotes 2D convolution. For simplicity, we neglected the magnification factor of the objective lens and the remaining parts of the derivatives in Eq.S26, which can be easily accounted for in actual implementation by rescaling the spatial coordinates. According to Eqs.S15 and S26, the intensity can be expanded into the following four components[13]:

$$I_1 = |U_{in}(x,y,0) * h(x,y)|^2 \tag{S27}$$

$$I_2 = [U_{in}(x,y,0) * h(x,y)]^* \cdot [U_S(x,y,0) * h(x,y)] \tag{S28}$$

$$I_3 = [U_{in}(x,y,0) * h(x,y)] \cdot [U_S(x,y,0) * h(x,y)]^* \tag{S29}$$

$$I_4 = |U_S(x,y,0) * h(x,y)|^2 \tag{S30}$$

where I_1 represents the DC term for the background intensity, and I_4 describes the nonlinear term for the second-order scattering interaction. If the sample and surrounding medium have a small RI contrast and weak absorption, this term can be neglected.

Under weak object approximation, we can discard the higher-order term I_4 to linearize Eq.S26:

$$I \approx I_1 + I_2 + I_3 \tag{S31}$$

Performing a 2D Fourier transform on Eqs.S27 and S28 yields:

$$\widehat{I_1}(k_x,k_y) = S(-k_{xi},-k_{yi}) \left|P(k_{xi},k_{yi})\right|^2 \delta(k_x - k_{xi}, k_y - k_{yi}) \tag{S32}$$

$$\begin{aligned}\widehat{I_2}(k_x,k_y) = &\frac{i}{2\pi} S(-k_{xi},-k_{yi}) P^*(k_{xi},k_{yi}) \\ &\int e^{ik_{zi}z'} \frac{e^{-\mathrm{i}\sqrt{k^2-(k_x+k_{xi})^2-\left(k_y+k_{yi}\right)^2}z'}}{\sqrt{k^2-(k_x+k_{xi})^2-(k_y+k_{yi})^2}} \widehat{O}\left(k_x,k_y,z'\right) P(k_x+k_{xi},k_y+k_{yi})\,\mathrm{d}z'\end{aligned} \tag{S33}$$

where P represents the pupil function of the objective lens, which is the 2D FT of the PSF. Also, since $I_3(x,y) = I_2^*(x,y)$, it follows:

$$\widehat{I_3}(k_x,k_y) = \widehat{I_2^*}(-k_x,-k_y) \tag{S34}$$

Next, we consider the scattering potential term:

$$O(\mathbf{r}) = \frac{1}{4\pi} k_0^2 \Delta\varepsilon(\mathbf{r}) \tag{S35}$$

where $\Delta\varepsilon(\mathbf{r}) = n(\mathbf{r}) - n_\mathrm{m}$ is the dielectric constant of the sample, representing local variations in the RI, and assuming $\varepsilon_n(\mathbf{r})$ is small, we can write the complex scattering potential O as:

$$O(\mathbf{r}) = k_0^2 \left[\Delta\varepsilon_{\mathrm{Re}} + i\Delta\varepsilon_{Im}\right] \tag{S36}$$

where $\Delta\varepsilon_{\mathrm{Re}}$ is the real part of $\varepsilon_n(\mathbf{r})$ and represents the phase effect on the object, $\Delta\varepsilon_{Im}$ is the imaginary part of $\varepsilon_n(\mathbf{r})$ and represents the effect of absorption. Performing a 2D Fourier transform of the $O(\mathbf{r})$ along the z-axis yields:

$$\widehat{O}\left(k_x, k_y, z\right) = k_0^2 \left[\widehat{\Delta\varepsilon}_{\mathrm{Re}}\left(k_x, k_y, z\right) + i\widehat{\Delta\varepsilon}_{Im}\left(k_x, k_y, z\right)\right] \tag{S37}$$

Since both $\Delta\varepsilon_{\mathrm{Re}}$ and $\Delta\varepsilon_{\mathrm{Im}}$ are real, their 2D Fourier transforms satisfy:

$$\begin{cases} \widehat{\Delta\varepsilon}_{\mathrm{Re}}\left(k_x, k_y, z\right) = \widehat{\Delta\varepsilon}_{\mathrm{Re}}^{*}\left(-k_x, -k_y, z\right) \\ \widehat{\Delta\varepsilon}_{\mathrm{Im}}\left(k_x, k_y, z\right) = \widehat{\Delta\varepsilon}_{\mathrm{Im}}^{*}\left(-k_x, -k_y, z\right) \end{cases} \tag{S38}$$

Therefore:

$$\widehat{O}^{*}\left(-k_x, -k_y, z\right) = k_0^2 \left(\widehat{\Delta\varepsilon}_{\mathrm{Re}}\left(k_x, k_y, z\right) - i\widehat{\Delta\varepsilon}_{Im}\left(k_x, k_y, z\right)\right) \tag{S39}$$

Substituting Eqs.S33, S34, S37 and S39 into Eq.S31, we can obtain the following Fourier domain linear model[14]:

$$\widehat{I} \approx \widehat{I}_1 + H_p\widehat{\Delta\varepsilon}_{\mathrm{Re}} + H_a\widehat{\Delta\varepsilon}_{\mathrm{Im}} \tag{S40}$$

where, H_p and H_a represent the phase and absorption transfer functions respectively. This model relates the intensity images captured from different illumination angles to the dielectric constant of the sample.

Then, calculate the spectrum $\widehat{I}_S = \widehat{I}_2 + \widehat{I}_3$ of the scattered field. To derive the phase and absorption transfer functions, we group all terms in $\widehat{I}_S$ containing $\widehat{\Delta\varepsilon}_{\mathrm{Re}}$ as $\widehat{I}_{S,\mathrm{Re}}$ and terms containing $\widehat{\Delta\varepsilon}_{\mathrm{Im}}$ as $\widehat{I}_{S,\mathrm{Im}}$[13–15]:

$$\widehat{I}_{S,\mathrm{Re}}(k_x,k_y)=\frac{\mathrm{i}k_0^2}{16\pi^3}S(-k_{xi},-k_{yi})$$
$$\int\left[P^*(k_{xi},k_{yi})\,e^{\mathrm{i}k_{zi}z'}\frac{e^{-\mathrm{i}\sqrt{k^2-(k_x+k_{xi})^2-\left(k_y+k_{yi}\right)^2}z'}}{\sqrt{k^2-(k_x+k_{xi})^2-\left(k_y+k_{yi}\right)^2}}P(k_x+k_{xi},k_y+k_{yi})\right. \tag{S41}$$
$$\left.-P(k_{xi},k_{yi})\,e^{-\mathrm{i}k_{zi}z'}\frac{e^{\mathrm{i}\sqrt{k^2-(-k_x+k_{xi})^2-\left(-k_y+k_{yi}\right)^2}z'}}{\sqrt{k^2-(-k_x+k_{xi})^2-\left(-k_y+k_{yi}\right)^2}}P^*(-k_x+k_{xi},-k_y+k_{yi})\right]\widehat{\Delta\varepsilon_{\mathrm{Re}}}(k_x,k_y,z')\,\mathrm{d}z'$$

$$\widehat{I}_{S,\mathrm{Im}}(k_x,k_y)=-\frac{k_0^2}{16\pi^3}S(-k_{xi},-k_{yi})$$
$$\int\left[P^*(k_{xi},k_{yi})\,e^{\mathrm{i}k_{zi}z'}\frac{e^{-\mathrm{i}\sqrt{k^2-(k_x+k_{xi})^2-\left(k_y+k_{yi}\right)^2}z'}}{\sqrt{k^2-(k_x+k_{xi})^2-\left(k_y+k_{yi}\right)^2}}P(k_x+k_{xi},k_y+k_{yi})\right. \tag{S42}$$
$$\left.+P(k_{xi},k_{yi})\,e^{-\mathrm{i}k_{zi}z'}\frac{e^{\mathrm{i}\sqrt{k^2-(-k_x+k_{xi})^2-\left(-k_y+k_{yi}\right)^2}z'}}{\sqrt{k^2-(-k_x+k_{xi})^2-\left(-k_y+k_{yi}\right)^2}}P^*(-k_x+k_{xi},-k_y+k_{yi})\right]\widehat{\Delta\varepsilon_{\mathrm{Im}}}(k_x,k_y,z')\,\mathrm{d}z'$$

where Eqs.S41 and S42 allow us to define the phase and absorption transfer functions at a given illumination angle $(-k_{xi},-k_{yi})$ and specific depth z'. Thus, the intensity spectrum can be rewritten as:

$$\widehat{I}(k_x,k_y)=\widehat{I}_1(k_x,k_y)+\int H_p(k_x,k_y,z';k_{xi},k_{yi})\,\widehat{\Delta\varepsilon_{\mathrm{Re}}}(k_x,k_y,z')\,\mathrm{d}z' \tag{S43}$$
$$+\int H_a(k_x,k_y,z';k_{xi},k_{yi})\,\widehat{\Delta\varepsilon_{Im}}(k_x,k_y,z')\,\mathrm{d}z'$$

where, the phase transfer function $H_p(k_x,k_y,z';k_{xi},k_{yi})$ is:

$$H_p(k_x,k_y,z';k_{xi},k_{yi})=\frac{\mathrm{i}k_0^2}{16\pi^3}S(-k_{xi},-k_{yi})$$
$$\left\{P^*(k_{xi},k_{yi})\,e^{\mathrm{i}k_{zi}z'}\frac{e^{-\mathrm{i}\sqrt{k^2-(k_x+k_{xi})^2-\left(k_y+k_{yi}\right)^2}z'}}{\sqrt{k^2-(k_x+k_{xi})^2-\left(k_y+k_{yi}\right)^2}}P(k_x+k_{xi},k_y+k_{yi})\right. \tag{S44}$$
$$\left.-P(k_{xi},k_{yi})\,e^{-\mathrm{i}k_{zi}z'}\frac{e^{\mathrm{i}\sqrt{k^2-(-k_x+k_{xi})^2-\left(-k_y+k_{yi}\right)^2}z'}}{\sqrt{k^2-(-k_x+k_{xi})^2-\left(-k_y+k_{yi}\right)^2}}P^*(-k_x+k_{xi},-k_y+k_{yi})\right\}$$

And the absorption transfer function $H_a(k_x,k_y,z';k_{xi},k_{yi})$ is:

$$
\begin{aligned}
&H_a\left(k_x,k_y,z';k_{xi},k_{yi}\right)=-\frac{k_0^2}{16\pi^3}S\left(-k_{xi},-k_{yi}\right)\\
&\left\{P^*\left(k_{xi},k_{yi}\right)e^{\mathrm{i}k_{zi}z'}\frac{e^{-\mathrm{i}\sqrt{k^2-\left(k_x+k_{xi}\right)^2-\left(k_y+k_{yi}\right)^2}z'}}{\sqrt{k^2-\left(k_x+k_{xi}\right)^2-\left(k_y+k_{yi}\right)^2}}P\left(k_x+k_{xi},k_y+k_{yi}\right)\right.\\
&\left.+P\left(k_{xi},k_{yi}\right)e^{-\mathrm{i}k_{zi}z'}\frac{e^{\mathrm{i}\sqrt{k^2-\left(-k_x+k_{xi}\right)^2-\left(-k_y+k_{yi}\right)^2}z'}}{\sqrt{k^2-\left(-k_x+k_{xi}\right)^2-\left(-k_y+k_{yi}\right)^2}}P^*\left(-k_x+k_{xi},-k_y+k_{yi}\right)\right\}
\end{aligned}
\tag{S45}
$$

where the terms $S\left(-k_{xi},-k_{yi}\right)$ and $P\left(k_{xi},k_{yi}\right)$ represent the effects of the light source. Since our illumination source is temporally quasi-coherent, we can obtain normalized transfer functions by dividing their respective transfer functions by $\widehat{I_1}$, considering the defocus situation:

$$
\begin{aligned}
H_p(\mathbf{u})=\frac{\mathrm{i}k_0^2}{16\pi^3}&\left\{P\left(\mathbf{u}-\mathbf{u}_{in}\right)\frac{\exp\{-i[\eta(\mathbf{u}-\mathbf{u}_{in})-\eta(\mathbf{u}_{in})](z+\Delta d)\}}{\eta(\mathbf{u}-\mathbf{u}_{in})}\right.\\
&\left.-P\left(\mathbf{u}+\mathbf{u}_{in}\right)\frac{\exp\{i[\eta(\mathbf{u}+\mathbf{u}_{in})-\eta(\mathbf{u}_{in})](z+\Delta d)\}}{\eta(\mathbf{u}+\mathbf{u}_{in})}\right\}
\end{aligned}
\tag{S46}
$$

$$
\begin{aligned}
H_a(\mathbf{u})=\frac{k_0^2}{16\pi^3}&\left\{P\left(\mathbf{u}-\mathbf{u}_{in}\right)\frac{\exp\{-i[\eta(\mathbf{u}-\mathbf{u}_{in})-\eta(\mathbf{u}_{in})](z+\Delta d)\}}{\eta(\mathbf{u}-\mathbf{u}_{in})}\right.\\
&\left.+P\left(\mathbf{u}+\mathbf{u}_{in}\right)\frac{\exp\{i[\eta(\mathbf{u}+\mathbf{u}_{in})-\eta(\mathbf{u}_{in})](z+\Delta d)\}}{\eta(\mathbf{u}+\mathbf{u}_{in})}\right\}
\end{aligned}
\tag{S47}
$$

where $\mathbf{u}=(k_x,k_y,z)$ signifies the frequency and spatial domain coordinates, (k_x,k_y) represent the frequency domain coordinates, $\mathbf{u}_{in}=(k_{xi},k_{yi})$ represent the frequency of the incident field, $\eta(\mathbf{x})=\sqrt{k_0^2-|\mathbf{x}|^2}$ denotes the axial wave vector, $\eta\left(\mathbf{u}-\mathbf{u}_{in}\right)=\sqrt{k^2-\left(k_x+k_{xi}\right)^2-\left(k_y+k_{yi}\right)^2}$, Δd refers to the axial defocus distance. By discretizing the 3D sample along the z-axis, we represent the axial position as $z=m\Delta z$, where Δz is the axial sampling interval (i.e., the slice thickness), and m is the index of the slices distributed on the z-axis.

S4.3 Formula derivation for reconstruction

First, each intensity image is processed to remove the background. Subsequently, based on the transfer functions derived from the forward model, the difference between the actual and predicted measured values is minimized using the least-squares algorithm with the l_2-norm[16]. Notably, due to the limited angular range covered by the illumination and imaging optics, there is a "missing cone" along the axial dimension in both the phase and absorption transfer functions. Consequently, direct inversion will lead to high-frequency artifacts due to the lack of information. This issue can be effectively mitigated by applying a minimum total energy constraint with Tikhonov regularization[17]:

$$\min_{\widehat{\Delta\varepsilon}_{\mathrm{Re}},\widehat{\Delta\varepsilon}_{Im}} \sum_{l,\Delta d} \left\| \widehat{I} - H_p \widehat{\Delta\varepsilon}_{\mathrm{Re}} - H_a \widehat{\Delta\varepsilon}_{Im} \right\|_2^2 + \alpha \left\| \widehat{\Delta\varepsilon}_{\mathrm{Re}} \right\|_2^2 + \beta \left\| \widehat{\Delta\varepsilon}_{Im} \right\|_2^2 \tag{S48}$$

where $\|\cdot\|_2^2$ is the l_2-norm of the vector, α and β are the regularization parameters, $\widehat{I}$ is the Fourier transform of the normalized acquired intensity data, H_p and H_a are the phase and absorption transfer functions derived in **Section 4.2**. Setting the first derivative of Eq.S48 to zero yields a closed solution. However, since $\widehat{\Delta\varepsilon}_{\mathrm{Re}}$ and $\widehat{\Delta\varepsilon}_{\mathrm{Im}}$ are not real numbers, the first derivative of Eq.S48 cannot be directly calculated. Decompose $\widehat{\Delta\varepsilon}_{\mathrm{Re}}$ and $\widehat{\Delta\varepsilon}_{\mathrm{Im}}$ into their real and imaginary parts:

$$\begin{aligned} \widehat{\Delta\varepsilon}_{\mathrm{Re}} &= \widehat{\Delta\varepsilon}_{\mathrm{Re}}^{(\mathrm{Re})} + j\widehat{\Delta\varepsilon}_{\mathrm{Re}}^{(\mathrm{Im})} \\ \widehat{\Delta\varepsilon}_{\mathrm{Im}} &= \widehat{\Delta\varepsilon}_{\mathrm{Im}}^{(\mathrm{Re})} + j\widehat{\Delta\varepsilon}_{\mathrm{Im}}^{(\mathrm{Im})} \end{aligned} \tag{S49}$$

Eq.S48 can be written as:

$$\begin{aligned} \min_{\widehat{\Delta\varepsilon}_{\mathrm{Re}},\widehat{\Delta\varepsilon}_{Im}} \sum_{l,\Delta d} \Bigg\{ & \left\| \widehat{I} - H_p \widehat{\Delta\varepsilon}_{\mathrm{Re}}^{(\mathrm{Re})} - jH_p \widehat{\Delta\varepsilon}_{\mathrm{Re}}^{(\mathrm{Im})} - H_a \widehat{\Delta\varepsilon}_{\mathrm{Im}}^{(\mathrm{Re})} - jH_a \widehat{\Delta\varepsilon}_{\mathrm{Im}}^{(\mathrm{Im})} \right\|_2^2 \\ & + \alpha \left\| \widehat{\Delta\varepsilon}_{\mathrm{Re}}^{(\mathrm{Re})} + j\widehat{\Delta\varepsilon}_{\mathrm{Re}}^{(\mathrm{Im})} \right\|_2^2 + \beta \left\| \widehat{\Delta\varepsilon}_{\mathrm{Im}}^{(\mathrm{Re})} + j\widehat{\Delta\varepsilon}_{\mathrm{Im}}^{(\mathrm{Im})} \right\|_2^2 \Bigg\} \end{aligned} \tag{S50}$$

Then setting the first derivatives of the above equation for $\widehat{\Delta\varepsilon}_{\mathrm{Re}}^{(\mathrm{Re})}$, $\widehat{\Delta\varepsilon}_{\mathrm{Re}}^{(\mathrm{Im})}$, $\widehat{\Delta\varepsilon}_{\mathrm{Im}}^{(\mathrm{Re})}$ and $\widehat{\Delta\varepsilon}_{\mathrm{Im}}^{(\mathrm{Im})}$ to zero, we obtain:

$$\begin{cases} \left(2{H_p}^2 + 2\alpha\right) \widehat{\Delta\varepsilon}_{\mathrm{Re}}^{(\mathrm{Re})} + 2H_a H_p \widehat{\Delta\varepsilon}_{\mathrm{Im}}^{(\mathrm{Re})} - H_p \left(\widehat{I} + \widehat{I}^* \right) = 0 \\ \left(2{H_p}^2 + 2\alpha\right) \widehat{\Delta\varepsilon}_{\mathrm{Re}}^{(\mathrm{Im})} + 2H_a H_p \widehat{\Delta\varepsilon}_{\mathrm{Im}}^{(\mathrm{Im})} + jH_p \left(\widehat{I} - \widehat{I}^* \right) = 0 \\ \left(2{H_a}^2 + 2\beta\right) \widehat{\Delta\varepsilon}_{\mathrm{Im}}^{(\mathrm{Re})} + 2H_a H_p \widehat{\Delta\varepsilon}_{\mathrm{Re}}^{(\mathrm{Re})} - H_a \left(\widehat{I} + \widehat{I}^* \right) = 0 \\ \left(2{H_a}^2 + 2\beta\right) \widehat{\Delta\varepsilon}_{\mathrm{Im}}^{(\mathrm{Im})} + 2H_a H_p \widehat{\Delta\varepsilon}_{\mathrm{Re}}^{(\mathrm{Im})} + jH_a \left(\widehat{I} - \widehat{I}^* \right) = 0 \end{cases} \tag{S51}$$

After sorting out Eq.S51, we can get:

$$\begin{cases} \widehat{\Delta\varepsilon}_{\mathrm{Re}} = \dfrac{-\sum\limits_{l,\Delta d} H_p(l,\Delta d)\beta\widehat{I}[l,\Delta d]}{\sum\limits_{l,\Delta d}|H_a(l,\Delta d)|^2\alpha+\sum\limits_{l,\Delta d}\left|H_p(l,\Delta d)\right|^2\beta+\alpha\beta} \\ \widehat{\Delta\varepsilon}_{\mathrm{Im}} = \dfrac{-\sum\limits_{l,\Delta d} H_a(l,\Delta d)\alpha\widehat{I}[l,\Delta d]}{\sum\limits_{l,\Delta d}|H_a(l,\Delta d)|^2\alpha+\sum\limits_{l,\Delta d}\left|H_p(l,\Delta d)\right|^2\beta+\alpha\beta} \end{cases} \tag{S52}$$

After performing the inverse Fourier transform on Eq.S52, we can obtain a closed solution for the internal RI values of the sample as described in **section 2.3** of the main text.

Supporting Information S5. BP-TIDT reconstruction algorithm

The pipeline of the BP-TIDT reconstruction algorithm is shown in Fig. S3, the detailed workflow of which can be schematically described as follows: 1) By sequentially turning on the illumination units on the annular LED, we acquired the corresponding intensity images under each illumination angle and recorded two sets of image stacks with and without samples. 2) We calibrate the illumination angles, which results in the shift of transfer functions, and use the background intensity stacks for the background artifact removal. 3) Calculate the transfer functions based on the imaging system's parameters and the corrected illumination angles in Step 2. 4) Reconstruct to obtain the 3D RI tomographic images and perform 3D rendering.

Step 1: Image stacks acquisition and LED spectral calibration

As shown in Fig. S3 Step 1, the illumination units on the annular LED are turned on in sequence to generate plane waves with an illumination 0.65 NA from different angles. Each LED (WS2812B, SMD-5050) operates at approximately 200 mW, delivering spatially coherent and quasi-monochromatic illumination with a wavelength of 523 nm and an FWHM width of 26 nm. We used a spectrometer (CCS200/M, Thorlabs) to calibrate the LED's central wavelength and spectral width and obtained the LED's spectral curve.

During the experiment, the LEDs on the ring were sequentially illuminated, passing through the sample. Subsequently, the light carrying the sample's RI information passes through the objective lens and the optical path inside the microscope, exits from the light outlet, and enters the back-end SLM phase modulation and bi-plane parallel detection module. In Supplementary Material S1, we analyzed the selection of PTF-based defocus distance to generate the corresponding phase modulation pattern on the back-end SLM, aiming to produce optimal defocus distance modulation. The reflected beams in the $4f$ system were laterally displaced by angles to spatially separate and synchronously capture intensity images with different defocus distances on the camera's focal plane. In **Visualization S3**, we demonstrate the physical principles of the image generation process through animation to demonstrate the image acquisition process more clearly. Then, we collect corresponding intensity images at each

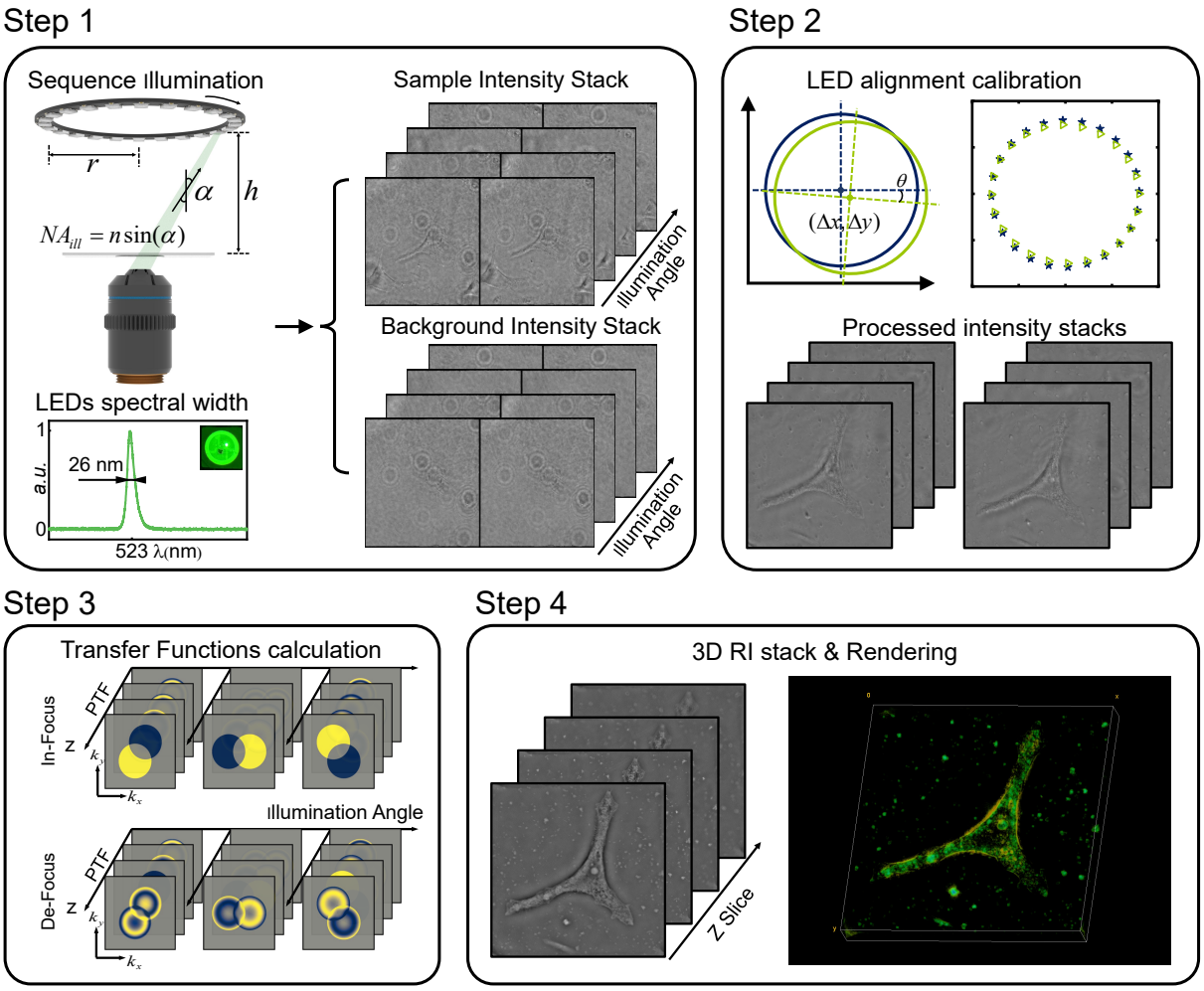

Figure S3. Pipeline of BP-TIDT reconstruction algorithm. Step 1: By sequentially turning on the illumination units on the annular LED, we acquired the corresponding intensity images under each illumination angle and recorded two sets of image stacks with and without samples (see also in **Visualization S3**). Step 2: Calibrate the illumination angles and use the background intensity stacks for the background artifact removal. Step 3: Calculate the transfer functions. Step 4: Reconstruct to obtain the 3D RI tomographic and perform 3D rendering.

illumination angle and record two sets of image stacks with and without the specimen. Note that the background image stack only needs to be measured once before placing the sample.

Step 2: Illumination angle calibration and intensity background normalization

For the LED illumination calibration process, we recorded 24 intensity images of pure phase objects on the in-focus plane, and the numerical self-calibration procedure of LED rings is performed in the frequency domain. The algorithm imposed here follows two geometric constraints. First, the distribution of our LED ring set is expected to obey concentric circular geometry. Second, the LEDs on each ring arrangement board are expected to be equally angled. Each pair of neighboring LEDs occupies a $2\pi/N$

radian, where $N = 24$ is the LED number. Our LED position calibration algorithm[18] starts with an initial guess (blue star in Step 2 of Fig. S3), and the initial estimated LED positions are often contaminated by noise. Accordingly, the final calibrated LED positions are parameterized as a nonlinear fitting between the raw calibration results and the circular geometry constraint of the LED ring set. By solving the optimization problem, the LED portion can be accurately calibrated, and the calibrated results are shown in Step 2 of Fig. S3.

As to the background normalization process, 24 raw intensity stacks of object $I_{Raw}(\mathbf{r})$ under illumination angles identical to the background data acquisition $I_B(\mathbf{r})$ are recorded within the same exposure time, and the background processed object intensity stacks are obtained by the normalization between raw intensity stack and background intensity distribution $I(\mathbf{r}) = I_{Raw}(\mathbf{r})/I_B(\mathbf{r})$. Note that background normalization is a mandatory step to compensate for the illumination inhomogeneities and ensure that the normalized illuminations from all LED elements are uniform and of unit amplitude. After background removal, the image is cropped and separated, and two sets of intensity stacks with different defocus distances are obtained, as shown in Step 2 of Fig. S3.

Step 3: Transfer Function calculation

The transfer function information can be obtained by bringing the calibrated LED center wavelength and spatial position information, as well as the basic parameters of the imaging system, into **Eq. 4** in **Section 2.2** of the main text. It is worth noting that if the parameters of the imaging system remain unchanged, then the transfer function does not need to be recalculated.

Step 4: 3D RI reconstruction and 3D rendering

By combining the two sets of defocused intensity stacks after removing the background in Step 2 and the transfer function calculated in Step 3 into **Eqs.7 and 8** in **section 2.3** of the main text, the 3D distribution of the sample's RI can be reconstructed. Finally, we used the Fiji software's volume viewer function to perform a 3D rendering of the sample, as shown in the Step 4 of Fig. S3.

Supporting Information S6. Hardware implementation for BP-TIDT

Our bi-plane parallel detection imaging system uses a Holoeye Pluto reflective liquid crystal pure phase panel as the spatial light modulator (SLM). This panel boasts a resolution of 1920×1080 pixels and a pixel size of 8 μm, enabling full 2π phase modulation with linear electro-optic characteristics. The SLM features 8-bit depth, which translates to 256 levels of grayscale, along with a reflectivity of up to 94% and an effective wavelength range spanning from 500 to 670 nm, adequately meeting the spectral requirements of our experiment. A linear polarizer is positioned in front of the SLM to maximize phase modulation efficiency, and a neutral density filter is employed to ensure uniform image brightness on the camera's sensor. It should be noted that, for the sake of clarity, these additional components are not depicted in **Fig. 1** of the main text. Pre-calibrating the SLM for phase modulation is essential before the

experiment commences. This process is critical for ensuring the precision and consistency of modulation throughout the experiment. By pre-calibrating, we can effectively compensate for the SLM's nonlinear phase response and static errors, thereby significantly enhancing the accuracy of wavefront control.

Although the SLM represents a higher-cost component within the experimental setup, its high resolution and phase modulation capabilities provide unique value to the experiment. The SLM allows us to precisely control the defocus distance and perform transfer function analysis, as shown in **Supporting Information S1**. Moreover, the phase modulation capability of the SLM permits the integration of aberration correction techniques into our experiment, enabling the correction of complex aberrations and further enhancing image quality[6]. The versatility and flexibility provided by the SLM offer advantages unmatched by other technologies. Therefore, despite the higher cost, using the SLM in this experiment is justified and necessary.

However, we also recognize that the SLM may be costly in some applications. There are some methods available to address the issue of cost-effectiveness. Blanchard et al.[19] placed a quadratically distorted grating before the imaging lens, creating three laterally shifted images corresponding to different defocus distances in a single image plane. Waller et al.[20] utilized the chromatic aberration inherent in the microscope to obtain three intensity images at different axial distances from a single color image. Martino et al.[21] developed a single-shot TIE setup based on a beam splitter and several mirrors, permitting recording two intensity images at different depths simultaneously.

Supporting Information S7. Supplementary experiment used 96 well plate sample chamber

High-throughput/high-content imaging is critical in biomedical research, providing detailed cellular information and rapid image analysis. It is essential to fundamental biological research, including drug screening, model organism studies, and cellular function analysis. As shown in Fig. S4(a), the 96-well plate is frequently used as a sample chamber in high-throughput/high-content imaging. These plates are designed with small well diameters and deep walls to maintain a nutrient-rich environment necessary for cell growth, which can limit the angle of light incidence. For instance, the 96-well plate in the figure allows a maximum illumination NA of 0.66. When the illumination NA surpasses this value, well walls may obstruct the light beam, causing a loss of image information, as shown in Fig. S4(b). This limitation can restrict the use of high NA objectives, such as 40× 0.95NA, with traditional ODT technology that requires matched illumination, thus affecting the imaging resolution in high-throughput/high-content applications.

The BT-TIDT method proposed in this article overcomes the lighting condition restrictions inherent in non-interferometric ODT technology. This advancement is compatible with standard sample chambers, such as the commonly used 96-well plates, for high-throughput/high-content imaging, allowing integration with existing laboratory setups. As demonstrated in Fig. S4(c), a 96-well plate was used

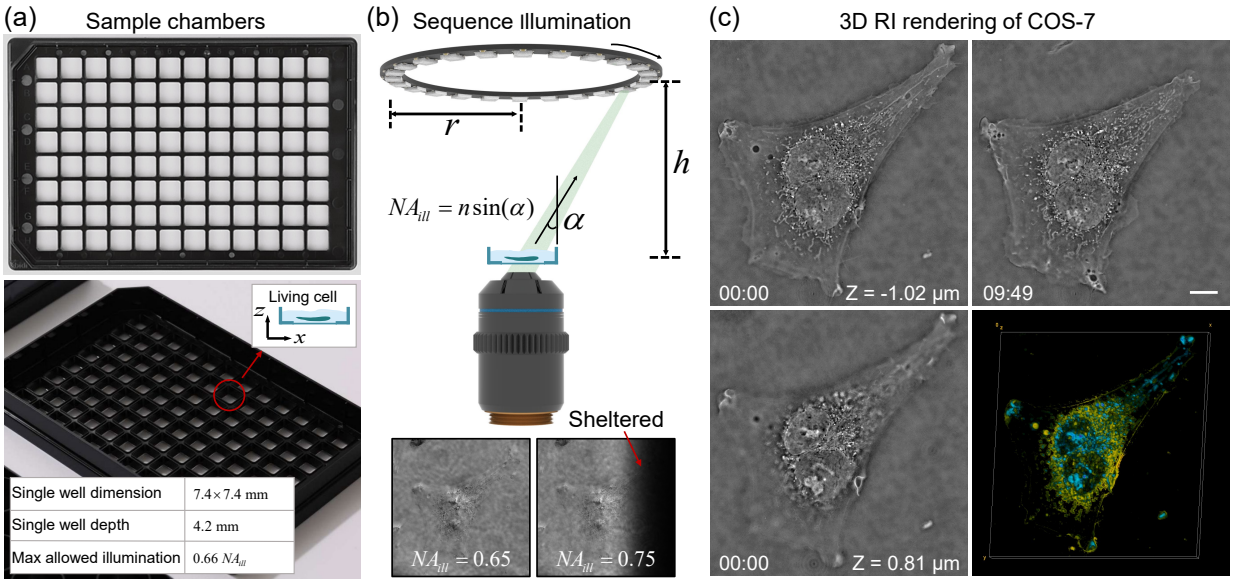

Figure S4. Compatibility analysis and imaging results of BP-TIDT method with 96 well plate sample chamber. (a) 96 well plate and its parameter information. (b) Principle of limited illumination angle and actual images of samples in well plates under different illumination angles (c) Results of High Speed and High-Resolution 3D RI Imaging of COS-7 Cells Using a 96-well Plate as a sample chamber (see **Visualization S4**).

for high-speed, high-resolution 3D refractive index (RI) imaging of COS-7 cells. The image displays a COS-7 cell in the division process, featuring two nuclei. Observations, including those in Fig. S4(c) and **Visualization S4**, indicate that pinocytosis at the cell's poles is evident during cell division, a period of high energy demand. This process is crucial for the cell's energy and material intake regulation. Additionally, as the cellular energy sources, mitochondria adopt elongated shapes for metabolic efficiency under low energy demand and become shorter and rounder to meet increased energy requirements during cell division. Further dynamic results and detailed visualizations are available in **Visualization S4**.

Our BT-TIDT method provides high-resolution and high-speed 3D imaging, serving as a valuable tool for high-throughput and high-content biological research. It is particularly beneficial for applications such as drug screening and molecular biology studies. This technology accelerates scientific discovery by facilitating detailed volumetric analysis of biological specimens with enhanced speed and resolution.

References

1. Jenkins, M. H. & Gaylord, T. K. Quantitative phase microscopy via optimized inversion of the phase optical transfer function. *Appl. Opt.* **54**, 8566–8579 (2015).
2. Zuo, C. *et al.* Transport of intensity equation: a tutorial. *Opt. Lasers Eng.* **135**, 106187 (2020).
3. Sung, Y. *et al.* Optical diffraction tomography for high resolution live cell imaging. *Opt. Express* **17**, 266–277 (2009).
4. Lim, J. *et al.* Comparative study of iterative reconstruction algorithms for missing cone problems in optical diffraction tomography. *Opt. Express* **23**, 16933–16948 (2015).
5. Zhou, N. *et al.* Single-exposure 3d label-free microscopy based on color-multiplexed intensity diffraction tomography. *Opt. Lett.* **47**, 969–972 (2022).
6. Shu, Y. *et al.* Adaptive optical quantitative phase imaging based on annular illumination fourier ptychographic microscopy. *PhotoniX* **3**, 24 (2022).
7. Li, J. *et al.* Transport of intensity diffraction tomography with non-interferometric synthetic aperture for three-dimensional label-free microscopy. *Light. Sci. & Appl.* **11**, 154 (2022).
8. Sun, J., Zuo, C., Zhang, J., Fan, Y. & Chen, Q. High-speed fourier ptychographic microscopy based on programmable annular illuminations. *Sci. Reports* **8**, 7669 (2018).
9. Zuo, C. *et al.* High-resolution transport-of-intensity quantitative phase microscopy with annular illumination. *Sci. Reports* **7**, 7654 (2017).
10. Wolf, E. Three-dimensional structure determination of semi-transparent objects from holographic data. *Opt. Commun.* **1**, 153–156 (1969).
11. Müller, P., Schürmann, M. & Guck, J. The theory of diffraction tomography. *arXiv preprint arXiv:1507.00466* (2015).
12. Soto, J. M., Rodrigo, J. A. & Alieva, T. Label-free quantitative 3d tomographic imaging for partially coherent light microscopy. *Opt. Express* **25**, 15699–15712 (2017).
13. Ling, R., Tahir, W., Lin, H.-Y., Lee, H. & Tian, L. High-throughput intensity diffraction tomography with a computational microscope. *Biomed. Opt. Express* **9**, 2130–2141 (2018).
14. Streibl, N. Three-dimensional imaging by a microscope. *JOSA A* **2**, 121–127 (1985).
15. Noda, T., Kawata, S. & Minami, S. Three-dimensional phase-contrast imaging by a computed-tomography microscope. *Appl. Opt.* **31**, 670–674 (1992).
16. Chowdhury, S. *et al.* High-resolution 3d refractive index microscopy of multiple-scattering samples from intensity images. *Opt.* **6**, 1211–1219 (2019).

17. Bertero, M., Boccacci, P. & De Mol, C. *Introduction to inverse problems in imaging* (CRC press, 2021).

18. Zhou, N. *et al.* Quasi-isotropic high-resolution fourier ptychographic diffraction tomography with opposite illuminations. *ACS Photonics* **10**, 2461–2466 (2023).

19. Blanchard, P. M., Fisher, D. J., Woods, S. C. & Greenaway, A. H. Phase-diversity wave-front sensing with a distorted diffraction grating. *Appl. Opt.* **39**, 6649–6655 (2000).

20. Waller, L., Kou, S. S., Sheppard, C. J. & Barbastathis, G. Phase from chromatic aberrations. *Opt. Express* **18**, 22817–22825 (2010).

21. Di Martino, J. M. *et al.* Single-shot phase recovery using two laterally separated defocused images. *Opt. Commun.* **293**, 1–3 (2013).